Journal of Materials Chemistry A

ROYAL SOCIETY OF CHEMISTRY

PAPER

View Article Online
View Journal

Cite this: DOI: 10.1039/d5ta10521h

From layer sliding to near-zero compressibility: novel high-pressure flexibility and CO_2 site evolution in pre-ELM-11 and ELM-11

Jingyan Liu, Julia M. Barker, Jiabin Xu, Yining Huang * and Yang Song *

Understanding how mechanical stress reshapes flexible metal–organic frameworks (MOFs) is important for designing robust, stimuli-responsive CO_2 sorbents. Here we compare the high-pressure flexibility of the elastic layered MOF ELM-11 and its hydrated precursor pre-ELM-11 using *in situ* synchrotron powder X-ray diffraction (PXRD) and Fourier-transform infrared (FTIR) spectroscopy. Pre-ELM-11 shows a pronounced change in anisotropic response at 2.15 GPa: compression along the *c* axis switches from positive linear compressibility (PLC) to negative linear compressibility (NLC), consistent with a transition from interlayer compression to pressure-driven layer sliding. In contrast, activated ELM-11 undergoes continuous anisotropic compression from 0.12 to 4.28 GPa dominated by interlayer contraction, and principal-axis analysis reveals near-zero linear compressibility (ZLC) along X3. To probe pressure-tuned host–guest interactions, we further monitor CO_2-loaded ELM-11 by *in situ* FTIR. Deconvolution of the ν_3 band of natural-abundance $^{13}CO_2$ resolves an increase in distinct adsorption environments from two to three at 3.44 GPa, with additional sites appearing above 9.59 GPa. Together, these results map distinct pressure-activated deformation pathways in closely related layered frameworks and demonstrate that mechanical pressure can reveal and create new CO_2 binding environments, informing the design of flexible 2D MOFs for pressure-responsive gas adsorption. More broadly, the comparative results identify interlayer hydrogen-bond pinning and initial interlayer spacing as key molecular levers that select pressure-activated deformation pathways and thereby tune pressure-dependent CO_2 site heterogeneity in layered flexible MOFs.

Received 26th December 2025
Accepted 15th March 2026

DOI: 10.1039/d5ta10521h

rsc.li/materials-a

Introduction

Metal–organic frameworks (MOFs) are widely explored for gas storage and separations, including CO_2 capture because their pore environments and chemical functionality can be systematically tuned.[1,2] For flexible MOFs, however, adsorption performance is inherently coupled to framework mechanics: modest changes in linker conformation or interlayer registry can reorganize pore apertures and binding environments. A key challenge is therefore to understand how mechanical stress reshapes flexible frameworks and their CO_2 host–guest interactions, in order to guide the design of stimuli-responsive yet robust sorbents. Hydrostatic compression provides a powerful and continuously tunable stimulus for probing such structure–property coupling, because pressure can systematically adjust framework geometry and thereby reshape MOF-CO_2 host–guest interactions.[3–24] Recent work has also demonstrated that temperature and/or pressure can be exploited as practical "knobs" to access high-selectivity regimes in crystals/MOFs, particularly for separations involving very similar molecules where conventional thermodynamic selectivity is limited.[25–28] In response to external pressure, in particular, two-dimensional (2D) layered MOFs are especially prone to anisotropic responses such as interlayer compression and layer sliding, which can yield anomalous mechanical phenomena including negative linear compressibility (NLC).[29–31] For example, NLC arising from pressure-induced layer sliding has been reported for 2D $Co(SCN)_2(pyrazine)_2$, highlighting the potential of layered frameworks for pressure-responsive functions such as sensing and actuation.[29]

Elastic layer-structured MOFs (ELMs) are a notable family of layered frameworks that display pronounced adsorption-induced flexibility. Among them, ELM-11 $[Cu(bpy)_2(BF_4)_2]$ (bpy = 4,4′-bipyridine) is a prototypical "gate-opening" CO_2 adsorbent in which guest uptake triggers cooperative structural reorganization associated with the BF_4^- anions and the layered lattice.[32–38] Despite extensive studies under gas pressure, the response of ELM-11 to external mechanical pressure—and how such deformation influences the diversity of CO_2 binding environments—remains largely unexplored. Its hydrated precursor, $[Cu(bpy)(H_2O)_2(BF_4)_2(bpy)]$, denoted pre-ELM-11 ref. 39 provides a chemically direct comparison point for isolating the role of hydration-enabled hydrogen bonding and interlayer

Department of Chemistry, University of Western Ontario, London, ON, N6A 5B7, Canada. E-mail: yhuang@uwo.ca; yang.song@uwo.ca

compliance in controlling high-pressure deformation pathways. Pre-ELM-11 and ELM-11 provide a closely related layered-framework pair that differs primarily by hydration state: pre-ELM-11 contains structural H_2O that participates in an interlayer hydrogen-bond network (involving BF_4^-), whereas dehydration yields ELM-11 with fully coordinated bpy layers and loss of interlayer hydrogen bonding (Fig. S1). Structural details are provided in the SI (Section S1).

Building on our previous high-pressure studies of diverse MOF platforms (*e.g.*, ZIF-8, MIL-68(In), CdSDB/PbSDB, MIL-53(Al), and $Zn_2(BDC)_2DABCO$), which revealed framework-dependent structural responses and CO_2 host–guest interactions under compression,[19–24] it is timely to extend such mechanistic investigations to flexible 2D layered MOFs, where anisotropic deformation (interlayer compression *versus* layer sliding) can dominate the response. Although ELM-11 has been extensively examined under gas pressure for various adsorbates,[40–42] an unresolved question is how fine chemical/structural tuning in layered MOFs selects the dominant deformation mode under hydrostatic pressure (interlayer contraction *vs.* shear/sliding) and how this pathway choice reshapes host–guest landscapes.

In this work, we directly address the above mechanism gap by reporting a comparative *in situ* high-pressure study of pre-ELM-11 and ELM-11 using synchrotron PXRD and FTIR spectroscopy to map their pressure-induced structural evolution and to connect framework chemistry (hydrogen bonding *versus* fully coordinated layers) to distinct deformation mechanisms. Quantitative analysis of anisotropic lattice strain enables direct comparison of compressibility directions and highlights how closely related layered frameworks can access markedly different mechanical responses under compression. More importantly, by linking pressure-activated layer mechanics to adsorption-site diversity, this work establishes hydrostatic pressure as a mechanistic probe and tuning variable for designing flexible layered MOFs with controllable CO_2 binding landscapes.

Experimental

Sample preparation

Pre-ELM-11 and ELM-11 were synthesised according to a reported procedure.[43] 4,4′-Bipyridine (0.312 g, 2.00 mmol) was dissolved in ethanol (2 mL) and added dropwise to an aqueous solution (8 mL) of $Cu(BF_4)_2 \cdot xH_2O$ (0.309 g, 1.00 mmol) at room temperature, accompanied by the immediate formation of a blue precipitate. The mixture was stirred for 2 h and then left undisturbed for 24 h. The resulting solid was collected by filtration, washed with ethanol, and air-dried for 2 h to afford blue powders (pre-ELM-11). Pre-ELM-11 was then activated under vacuum at 100 °C for 5 h to remove structural H_2O, yielding ELM-11. The samples were stored in an MBraun glovebox under a N_2 atmosphere (H_2O content < 0.1 ppm and O_2 content < 4.6 ppm). Phase purity of pre-ELM-11 and ELM-11 was confirmed by PXRD using Cu Kα radiation (λ = 1.5406 Å) (Fig. S2). For measurements outside the glovebox, ELM-11 was loaded into and sealed in glass capillaries to minimise exposure to ambient moisture and air.

In situ high-pressure microdiffraction

A diamond-anvil cell (DAC) equipped with a pair of type-I diamonds (400 μm culets) was utilised to generate static high pressure. A stainless-steel gasket was pre-indented to a thickness of ~70 μm and a 150 μm-diameter hole was drilled to form the sample chamber. A ruby chip was loaded into the chamber for pressure determination by ruby fluorescence. The samples were loaded together with silicone oil (PTM) in an MBraun glovebox to minimise interference from ambient moisture and air.

In situ angle-dispersive X-ray microdiffraction was performed at the High Energy Wiggler (WHE) beamline of the Brockhouse X-ray Diffraction and Scattering (BXDS) sector at the Canadian Light Source (CLS). The monochromatic X-ray beam had a wavelength of 0.3456 Å and was defined to a beam size of ~50 μm × 50 μm using a pinhole. The diffraction geometry was calibrated using a nickel powder standard. Two-dimensional Debye–Scherrer diffraction images were collected using a Varex XRD 4343CT area detector and integrated to one-dimensional patterns using Dioptas for subsequent analysis.[44] The resulting 1D patterns were analysed by Le Bail refinement using GSAS-II.[45] Synchrotron PXRD measurements were performed within limited beam time and therefore were not repeated for multiple independent loadings; however, the key observations (including the pronounced change in compression behaviour of pre-ELM-11 and the reversible recovery upon pressure release) were robust within the measured compression–decompression sequence.

In situ FTIR spectroscopy

For FTIR measurements, the samples were loaded into a DAC without a pressure-transmitting medium (PTM). A DAC equipped with type-II diamonds (600 μm culets) and a stainless-steel gasket (80 μm thickness; 210 μm chamber diameter) was used. When required to avoid saturated absorbance, pre-dried solid KBr was co-packed with the sample as an IR-transparent spacer. CO_2 was loaded using a cryogenic method. After loading ELM-11 (without KBr for CO_2-loading experiments) in an MBraun glovebox, the DAC was transferred to a Cleatech portable glovebox filled with N_2 to minimise H_2O contamination during loading and cooled below the sublimation temperature of dry ice (~−78 °C) using a liquid-nitrogen bath whereas N_2/O_2 remain gaseous. Excess high-purity CO_2 gas was introduced and condensed into the sample chamber, followed by rapid sealing and compression to an initial pressure of ~0.1 GPa. Upon warming to room temperature, a sealed system containing CO_2-loaded ELM-11 and excess free CO_2 was obtained. For the control experiment with pure CO_2, the same loading process was performed without the MOF.

In situ FTIR spectra were recorded using a customised IR microspectroscopy setup. A Bruker Vertex 80v FTIR spectrometer equipped with a Globar IR source was operated under vacuum (<5 mbar) to minimise atmospheric H_2O and CO_2

interference. Using the diamond anvils' absorption as the background, spectra were collected in transmission mode at 4 cm^{-1} resolution, averaging 512 scans per measurement.

Multi-cycle mechanical testing (repeated compression–decompression loops within a single DAC loading) was not performed, because DAC gaskets typically undergo irreversible plastic deformation during compression, which alters the sample-chamber geometry and makes strict cycling under identical conditions difficult. Instead, reproducibility was assessed by (i) recording compression and subsequent decompression data to verify recovery of diffraction patterns/spectra, and (ii) repeating the *in situ* FTIR compression–decompression experiments multiple times (independent measurements) for each sample to confirm that the key spectral trends are reproducible.

Results and discussion

Pressure-induced two-stage compression of pre-ELM-11

In situ synchrotron PXRD patterns of pre-ELM-11 were collected from 0.20 to 5.60 GPa to track pressure-induced structural changes (Fig. 1a). The pattern measured at 0.20 GPa is consistent with the simulated diffraction pattern converted to the same wavelength.[39] With increasing pressure up to 2.15 GPa, all reflections exhibit a continuous shift to higher 2θ, consistent with overall lattice contraction. Above 2.15 GPa, several

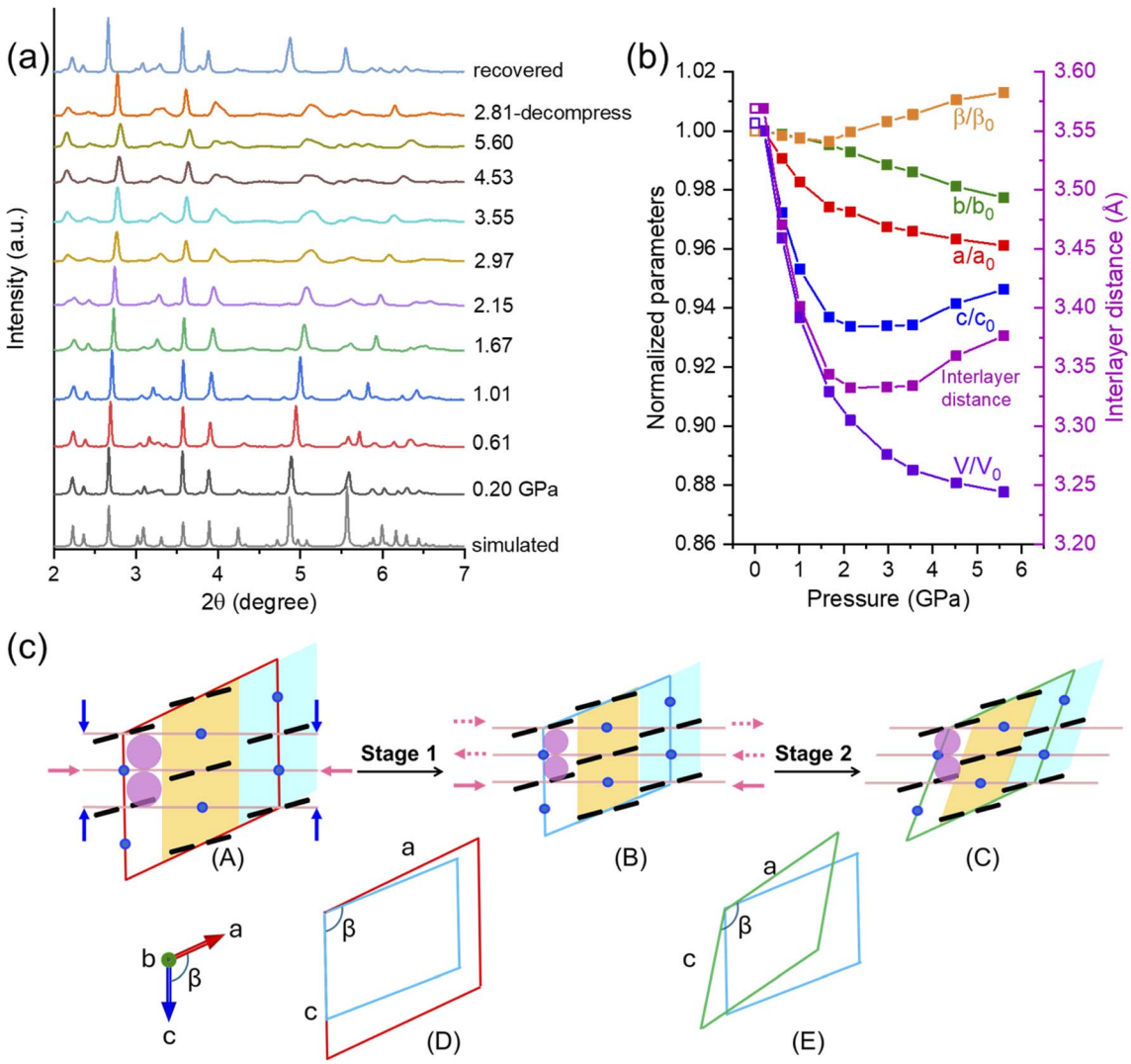

Fig. 1 (a) *In situ* synchrotron PXRD patterns of pre-ELM-11 collected on compression from 0.20 to 5.60 GPa and after decompression. (b) Pressure dependence of the normalised unit-cell parameters (*a*, *b*, *c*), unit-cell volume (*V*), and interlayer distance of pre-ELM-11; filled squares denote compression and open squares denote recovered data after pressure release. (c) Schematic representation of the two-stage lattice response of pre-ELM-11: (A) ambient-pressure structure (simplified from Fig. S1b), (B) compressed structure at the end of Stage 1 (interlayer-dominated compression), and (C) Stage-2 sliding-assisted deformation above the ~2.15 GPa crossover. Unit cell deformations for Stage 1 comparing before and after deformation (D) and for Stage 2 (E) are illustrated schematically (not to scale; exaggerated for clarity). Cu atoms are shown as blue spheres and bpy units as black sticks; layers are indicated by pink lines. Interlayer space is indicated by pink spheres. Blue arrows denote interlayer compression, solid pink arrows denote intralayer compression, and dashed pink arrows denote relative layer translation (sliding vector).

reflections split, become nearly stationary, or shift slightly to lower 2θ, indicating a change in the compression behaviour. Upon decompression to ambient pressure, the diffraction pattern returns close to its initial form, demonstrating excellent reversibility up to 5.60 GPa.

The lattice parameters at each pressure were obtained by Le Bail refinement using the reported crystallographic model in space group $C2/c$.[39] The refined lattice parameters and unit-cell volume are shown in Fig. S3a–c, and their normalised values are summarised in Fig. 1b. The data reveal a two-stage anisotropic response separated at 2.15 GPa, most clearly reflected in the behaviour of the c axis. Up to 2.15 GPa, the framework contracts predominantly along c, whereas above 2.15 GPa c increases slightly (*i.e.*, a weak NLC response), accompanied by an attenuated contraction of a. In contrast, b decreases gradually throughout the full 0.20–5.60 GPa range. The monoclinic angle β decreases slightly up to 1.67 GPa and then increases continuously (Fig. S3b and 1b). To quantify the associated stiffening, the pressure–volume data for each stage were fitted separately using EoSFit7 [46] with a third-order Birch–Murnaghan equation of state (Fig. S3c). The fitted bulk modulus K_0 increases from 8.9 GPa (stage 1) to 49.6 GPa (stage 2), indicating a marked reduction in compressibility above 2.15 GPa.

The mechanism of the two-stage compression—particularly the onset of weak NLC along c above 2.15 GPa—was analysed in the context of the ambient-pressure structure of pre-ELM-11 (Fig. S1a and b). The b axis lies within the 2D layers, aligned with the direction of the Cu(II)-bpy coordination chains, whereas c is approximately normal to the layers and a lies closer to the layer plane. Because β changes only modestly over the measured pressure range, the orientations of the lattice axes relative to the layers are expected to remain approximately comparable during compression. Accordingly, the pronounced contraction of c in stage 1 is consistent with dominant interlayer compression, while the more moderate contraction of a reflects intralayer deformation enabled by the non-coordinated bpy and hydrogen bonding (O–H···N). In contrast, the coordinated bpy chains impart greater rigidity along b, consistent with its relatively small and continuous contraction.

As illustrated schematically in Fig. 1c, the combined effects of interlayer and intralayer compression produce the stage-1 structure (B), with shortened c and a and a slight decrease in β relative to the ambient structure (A). The interlayer distance (defined from the lattice geometry and layer orientation; Fig. 1b) decreases in parallel with c and reaches 3.33 Å at 2.15 GPa, suggesting limited scope for further reduction without incurring significant steric repulsion between closely stacked layers. This constraint may activate an alternative deformation mode, most plausibly lateral layer translation (sliding), as reported in other layered MOFs under hydrostatic pressure.[29] In the stage-2 schematic (Fig. 1c, C), layer sliding combined with continued intralayer compression can account for the observed trends: a continues to decrease slightly, β increases, and c shows a small recovery (weak NLC). Overall, the PXRD-derived lattice evolution is therefore consistent with a crossover from interlayer-dominated compression to a sliding-assisted mechanism at ~2.15 GPa.

To complement the long-range lattice evolution identified by PXRD, we used *in situ* FTIR spectroscopy to probe local bonding changes in pre-ELM-11 under compression, particularly those involving structural H_2O and the BF_4^--mediated hydrogen-bond network. A representative spectrum collected at 0.44 GPa is shown in Fig. S4, and peak assignments are summarised in Table S1. The pressure-dependent spectra in the 600–1700 cm^{-1} region (dominated by bpy and BF_4^- modes) are presented in Fig. S5, while the ν(OH) stretching region of the structural H_2O is highlighted in Fig. 2a. Notably, the ν(OH) band splits into a doublet at 1.62 GPa, consistent with –OH groups participating in at least two hydrogen-bonding environments (O–H···F and O–H···N). With increasing pressure, the bands generally shift to higher wavenumber (blue shift) and broaden, consistent with progressive bond stiffening under compression. Upon decompression, the spectra recover to near their initial forms, indicating reversible behaviour up to 10.52 GPa.

To further resolve pressure-driven changes in the structural-water hydrogen-bonding environments, the ν(OH) region was deconvoluted (Fig. S6), and the relative areas of each component are summarised in Table S2. At 0.53 GPa, two components are observed: the lower-frequency band, ν(OH)_1, and the higher-frequency band, ν(OH)_2. These are assigned to –OH groups engaged primarily in O–H···F and O–H···N interactions, respectively, consistent with the stronger red-shifting influence typically associated with hydrogen bonding to F relative to N. The ν(OH)_1 and ν(OH)_2 populations remain approximately 1 : 1 from 0.53 to 2.75 GPa. A third, higher-frequency component, ν(OH)_3, emerges at 3.90 GPa and increases steadily with pressure, while ν(OH)_2 remains close to ~50%, suggesting that ν(OH)_3 grows primarily at the expense of ν(OH)_1. This redistribution is consistent with a pressure-induced reorganisation/weakening of a subset of O–H···F interactions in the higher-pressure regime, in line with the PXRD-inferred crossover from interlayer-dominated compression to a sliding-assisted mechanism.

To quantify the pressure response of the vibrational modes and assess stage-dependent changes in local bonding sensitivity to pressure, the peak positions of the main IR bands (including the ν(OH) doublet components) were plotted and fitted linearly within each pressure regime (Fig. 2b and c). The broad and strongly overlapped ν_as (B–F) band was excluded from this analysis. The resulting pressure coefficients ($d\nu/dP$, cm^{-1} GPa^{-1}) are labelled in Fig. 2b and c. Notably, most modes exhibit two distinct linear regimes (0.53–2.75 GPa and 3.90–10.52 GPa), with reduced pressure coefficients at higher pressure, indicating a lower pressure sensitivity of the local vibrational environments. This trend is consistent with the PXRD-derived crossover to a stiffer response above ~2.15 GPa.

As shown in Fig. 2b, the ν(OH) components display relatively large positive pressure coefficients (16.4 and 14.9 cm^{-1} GPa^{-1}) in the 0.53–2.75 GPa regime, corresponding to a pronounced blue shift of the O–H stretching bands. Such positive shifts suggest that compression increases the effective O–H stretching force constant, consistent with a dominant contribution from covalent O–H stiffening and/or pressure-induced reorganisation (or weakening) of a subset of O–H···X hydrogen bonds. In

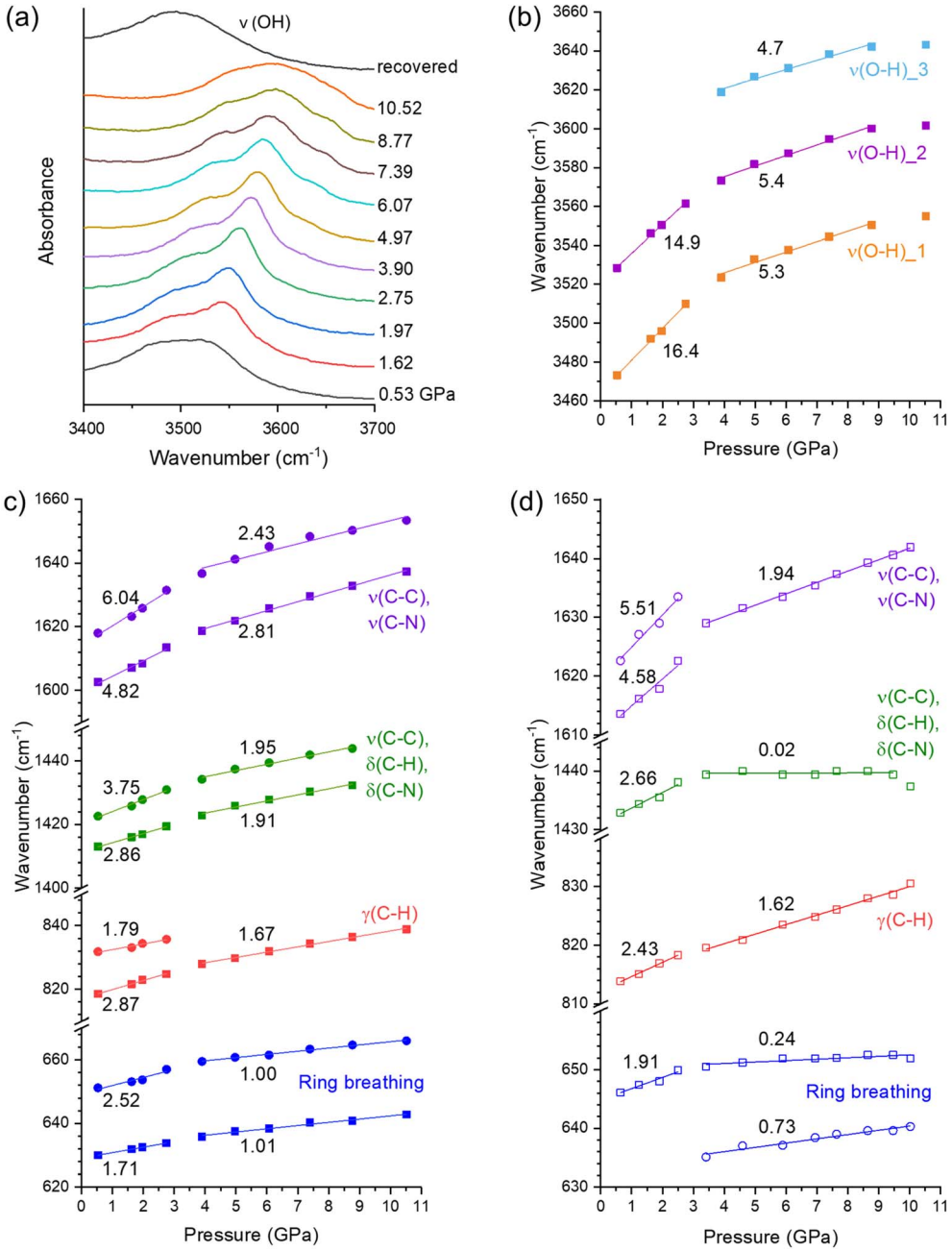

Fig. 2 (a) Selected *in situ* FTIR spectra of pre-ELM-11 in the ν(OH) stretching region (3400–3700 cm^{-1}) collected on compression and decompression. (b) Pressure dependence of the ν(OH) component frequencies of pre-ELM-11 (3460–3660 cm^{-1}). (c) Pressure dependence of selected pre-ELM-11 framework vibrational modes in the 620–1660 cm^{-1} region. (d) Pressure dependence of selected ELM-11 framework vibrational modes in the 630–1650 cm^{-1} region. Where shown, lines represent linear fits within each pressure regime and labels give pressure coefficients ($d\nu/dP$, cm^{-1} GPa^{-1}).

contrast, strengthening of hydrogen bonding typically leads to a red shift, indicating that hydrogen-bond shortening is not the dominant spectral driver for ν(OH) in this pressure range.

Pressure-induced continuous compression of ELM-11

In situ synchrotron PXRD patterns of ELM-11 were collected from 0.12 to 4.28 GPa to probe pressure-induced structural changes (Fig. 3a). The pattern measured at 0.12 GPa shows good agreement with the simulated ambient-pressure pattern.[38] With increasing pressure, the reflections shift continuously to higher 2θ to varying extents, consistent with anisotropic lattice contraction. Although the peaks gradually broaden with increasing pressure, most of the principal reflections remain visible, indicating that crystallinity is largely retained up to 4.28 GPa. Upon decompression to ambient pressure, most reflections return close to their initial positions, demonstrating excellent reversibility over this pressure range.

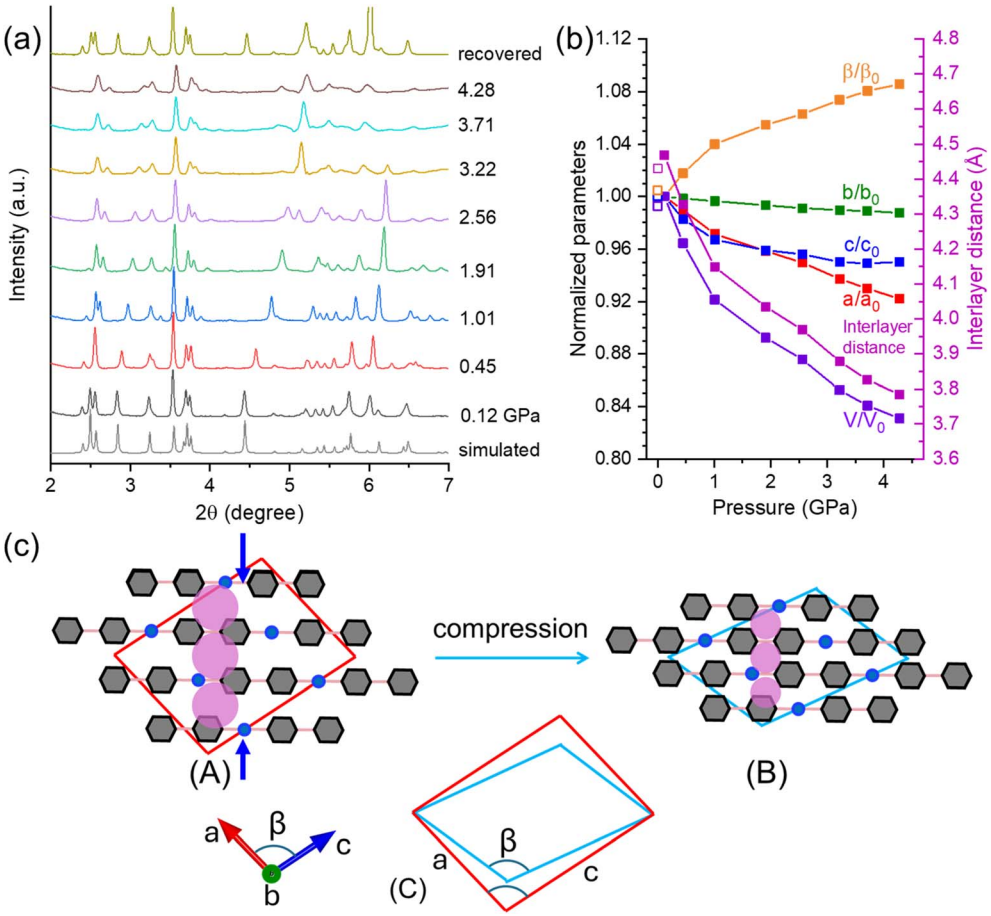

Fig. 3 (a) *In situ* synchrotron PXRD patterns of ELM-11 collected on compression from 0.12 to 4.28 GPa and after decompression. (b) Pressure dependence of the normalised unit-cell parameters (*a*, *b*, *c*), unit-cell volume (*V*), and interlayer distance of ELM-11; filled squares denote compression and open squares denote recovered data after pressure release. (c) Schematic illustration of the lattice response of ELM-11 dominated by interlayer compression: (A) ambient-pressure structure (simplified from Fig. S1d) and (B) compressed structure. Unit cell deformations before and after deformation (C) are illustrated schematically (not to scale; exaggerated for clarity). Cu atoms are shown in blue and bpy units in black; layers are indicated by pink lines. Blue arrows and the change in size of pink spheres indicate the decrease in interlayer spacing, which dominates the deformation over 0.12–4.28 GPa.

The lattice parameters and unit-cell volume of ELM-11 at each pressure were determined by Le Bail refinement using the reported crystallographic model in space group $C2/c$[38] (Fig. S7a–c). Over the compression range of 0.12–4.28 GPa, the lattice parameters *a*, *b*, and *c* all decrease continuously, while the monoclinic angle β increases. The pressure–volume data are well described by a third-order Birch–Murnaghan equation of state, yielding a bulk modulus $K_0 = 6.7$ GPa. The corresponding normalised lattice parameters and volume are summarised in Fig. 3b to compare relative change amplitudes. The largest contraction occurs along *a* and *c* at lower pressures; however, above ~1.91 GPa the rate of decrease in *c* becomes noticeably attenuated, resulting in a reduced overall change in *c*. In contrast, the *b* axis contracts only slightly and monotonically across the full pressure range, similar to pre-ELM-11. Compared with pre-ELM-11, β shows a more pronounced change, increasing by >8% over 0.12–4.28 GPa.

This compression process was further analysed based on the reported ambient-pressure crystal structure of ELM-11 (Fig. S1c and d).[38] Upon removal of structural H_2O, all bpy linkers coordinate to Cu(II), forming the quasi-square 2D grid layers (Fig. S1c). As in pre-ELM-11, the crystallographic *b* axis lies along one direction of the rigid bpy linkers, consistent with the small, monotonic contraction of *b* upon compression (Fig. 3b). In contrast, neither the *a* nor *c* axis is aligned with the layer plane or the layer normal, so changes in *a*, *c*, and β jointly determine how the interlayer separation evolves with pressure. Using the geometric relationship between the lattice parameters and the layer orientation, we calculated the interlayer distance (Fig. 3b), which decreases continuously by ~15% at 4.28 GPa, substantially larger than the maximum reduction observed for pre-ELM-11 (~7% at 2.15 GPa, Fig. 1b). Unlike the two-stage response of pre-ELM-11, the continuous decreases in unit-cell volume and interlayer distance indicate that interlayer compression dominates the response of ELM-11 throughout 0.12–4.28 GPa (Fig. 3c). The accompanying increase in β implies that the projection of interlayer contraction onto the crystallographic axes evolves with pressure, providing a geometric

rationale for the attenuated decrease of c above ~1.91 GPa even as the interlayer distance continues to shrink. While intralayer compression and/or minor sliding cannot be excluded, their contributions appear secondary within this pressure range. The larger initial interlayer spacing and absence of interlayer hydrogen bonding in ELM-11 likely facilitate the greater degree of interlayer contraction observed here. To describe this anisotropic deformation in physically meaningful directions relative to the layers, we next analyse the principal-axis strains using PASCal.

Because the crystallographic axes are not aligned with the layer normal/plane in ELM-11, the anisotropic deformation was analysed using principal-axis strains. The principal axes (X_1, X_2, X_3) and corresponding principal strains (ε_1, ε_2, ε_3) were computed using PASCal and are summarised in Table S3 and Fig. S8a, respectively.[47] In this representation, X_2 coincides with the crystallographic b axis, while X_1 and X_3 lie in the ac plane and are oriented approximately normal to and within the 2D layers, respectively. The pressure-dependent principal strains were fitted using the empirical strain–pressure model implemented in PASCal,[47] and the corresponding pressure-dependent linear compressibilities (K_1, K_2, K_3) were derived from the fitted strain curves (Fig. S8b). As expected for a layered framework dominated by interlayer contraction, K_1 is the largest, decreasing from 181.0 TPa^{-1} at 0.12 GPa to 26.6 TPa^{-1} at 1.91 GPa, and then to 15.3 TPa^{-1} at 4.28 GPa. The in-plane response is much smaller: K_2 decreases gradually from 5.0 to 1.9 TPa^{-1} between 0.12 and 4.28 GPa, while K_3 decreases from 4.1 to 0.9 TPa^{-1} over the same range. To visualise the anisotropy, the linear-compressibility indicatrix at 1.91 GPa is shown in Fig. S8c, where the radial distance represents the magnitude of linear compressibility in a given direction; the strongest response is clearly along X_1, nearly perpendicular to the layers. These results corroborate interlayer compression as the dominant deformation mode in the 0.12–4.28 GPa range. Notably, K_2 and K_3 fall below typical values for crystalline materials (5–20 TPa^{-1}),[48] and K_3 approaches the near-ZLC regime, being comparable to that of diamond (~0.75 TPa^{-1}).[49,50] The combined behaviour of X_2 and X_3 also suggests potential zero area compressibility (ZAC) in the X_2–X_3 plane at higher pressures. Materials exhibiting ZLC/ZAC can maintain a nearly constant dimension (or area) under compression, a rare balance that is attractive for applications requiring dimensional stability, including pressure-sensing and actuation functionalities.[51–53]

A representative FTIR spectrum of ELM-11 collected at 0.64 GPa is shown in Fig. S4, with peak assignments summarised in Table S1. The *in situ* FTIR spectra of ELM-11 collected over 0.64–10.02 GPa are shown in Fig. S9. With increasing pressure, most bands exhibit gradual blue shifts and broadening, and several modes show clear changes in band shape. In particular, the ν(C–C)/ν(C–N) doublet near ~1620 cm^{-1} coalesces into a single broad band at 3.41 GPa, while the ring-breathing mode at 646 cm^{-1} begins to split at a similar pressure. All spectral features recover upon decompression, indicating excellent reversibility up to 10.02 GPa.

To quantify the pressure response, peak positions of the main bands (excluding the broad, overlapped ν_as(B–F) feature) were plotted and fitted linearly as a function of pressure (Fig. 2d), yielding pressure coefficients $d\nu/dP$ (cm^{-1} GPa^{-1}). As for pre-ELM-11, most modes show a discontinuity in $d\nu/dP$, occurring here near ~3–3.5 GPa, and the pressure coefficients are generally smaller at higher pressure (3.41–10.02 GPa) than at lower pressure (0.64–2.50 GPa). This reduction is especially pronounced for bpy skeletal modes (ring breathing, ν(C–C)/δ(C–H)/δ(C–N), and ν(C–C)/ν(C–N)), indicating reduced pressure sensitivity and increased rigidity of these local environments in the higher-pressure regime. Unlike pre-ELM-11, ELM-11 contains fully coordinated bpy linkers and a more compact intralayer configuration after dehydration (Fig. S1c),[35,38] in which several pyridine rings tilt out of the layer plane (Fig. S1d). Under compression, interlayer contraction can initially be accommodated by torsional adjustments (ring rotation),[54,55] which may contribute to the observed splitting/merging behaviour at lower pressures. As pressure increases toward ~3 GPa, decreasing interlayer separation can restrict this rotational freedom, consistent with both the spectral-shape changes and the reduced $d\nu/dP$ values of the bpy modes above ~3.4 GPa.

Taken together, these results show how dehydration fundamentally rewires the high-pressure mechanics of this layered framework family. In pre-ELM-11, interlayer and intralayer hydrogen bonding (O–H···F and O–H···N) enforce tight stacking that initially accommodates pressure by interlayer compression and then, beyond ~2.15 GPa, activates lateral layer translation (sliding), giving rise to weak NLC along c and a marked stiffening response. By contrast, removal of structural H_2O in ELM-11 eliminates interlayer hydrogen bonding, increases the initial interlayer spacing, and yields a fully coordinated bpy network; the framework therefore responds predominantly by continuous interlayer compression over 0.12–4.28 GPa, with principal-axis analysis locating the maximum compressibility nearly normal to the layers and near-ZLC along X_3. The IR signatures mirror these distinct pathways: pre-ELM-11 shows stage-dependent ν(OH) evolution consistent with hydrogen-bond reorganisation, whereas ELM-11 exhibits pressure-dependent changes in bpy skeletal modes that become markedly less pressure-sensitive above ~3–3.5 GPa, consistent with restricted torsional accommodation at reduced layer spacing. Overall, hydrogen-bond topology and initial interlayer distance emerge as key levers controlling whether compression proceeds *via* sliding (pre-ELM-11; NLC) or sustained interlayer contraction with near-ZLC (ELM-11).

The comparative behavior of pre-ELM-11 and ELM-11 illustrates a transferable structure–mechanics relationship for layered MOFs under hydrostatic compression. When interlayer coupling is strengthened by structural water and an extended hydrogen-bond network (pre-ELM-11), interlayer distance reduction is accommodated only up to a steric/packing limit, after which shear-type deformation (layer sliding) becomes the lower-energy pathway, producing a marked stiffening and the observed compressibility crossover. By contrast, removing structural H_2O eliminates interlayer hydrogen bonding and increases interlayer compliance (ELM-11), favoring continuous

interlayer contraction and enabling exceptionally small compressibility along a principal axis. These results suggest a practical design rule: interlayer "pinning" interactions (H-bonding, strong interlayer contacts) promote pressure-activated sliding once normal compression saturates, whereas reducing interlayer pinning favors sustained contraction and near-zero-compressibility regimes.

Pressure-induced guest–host interactions of CO_2-Loaded ELM-11

With the compression pathways established, a key question is whether external pressure can reorganise host–guest interactions and reveal additional CO_2 binding environments in ELM-11. To address this, we collected *in situ* FTIR spectra of CO_2-loaded ELM-11 from 0.29 to 10.27 GPa (Fig. S10), where new bands assigned to CO_2 (ν_2, ν_3, and combination modes) appear alongside framework vibrations. Because several absorptions become saturated under these conditions, only four unsaturated framework modes were tracked and fitted as a function of pressure (Fig. S11) to obtain pressure coefficients, $d\nu/dP$ (cm^{-1} GPa^{-1}), as an indicator of spectroscopic pressure sensitivity. The γ(C–H) mode varies continuously over the full pressure range, whereas the other three modes exhibit a clear change in slope at ~7 GPa, substantially higher than the ~3–3.5 GPa discontinuity observed for guest-free ELM-11 (Fig. 2d). Moreover, the reduction in $d\nu/dP$ above the threshold is less pronounced than in the guest-free framework, indicating that CO_2 inclusion maintains a more pressure-sensitive (apparently "softer") local environment at higher pressures. This behaviour is consistent with the reported two-step gate-opening phenomenon, in which saturated adsorption of fluid CO_2 near ambient conditions can expand the interlayer distance of ELM-11 by ~56%;[42] the resulting larger layer spacing may provide additional capacity for interlayer contraction even when the channels are occupied by CO_2. In addition, δ(C–H) splits at 4.65 GPa, which may signal a pressure-induced change in the local framework environment and/or host–guest interactions. We therefore analyse the CO_2 combination bands and the natural-abundance $^{13}CO_2$ ν_3 mode below to resolve adsorption-site evolution with pressure.

To further probe pressure-dependent host–guest interactions, the CO_2 combination bands are enlarged in Fig. 4a. Upon compression to 1.31 GPa, each combination band splits into two components, consistent with solidification of excess CO_2 in the sample chamber (outside the framework pores). By comparison with pure solid CO_2 at 1.11 GPa, the higher-wavenumber components of both combination bands are assigned to solid CO_2 outside the framework, whereas the lower-wavenumber components are attributed to CO_2 confined within ELM-11. With increasing pressure, the bands exhibit gradual blue shifts and broadening. Notably, the confined-CO_2 components become progressively asymmetric from 3.44 GPa, consistent with the emergence of multiple adsorption environments at elevated pressure.

A similar behaviour is observed for the natural-abundance $^{13}CO_2$ ν_3 band (Fig. 4b). The ν_3 band also splits at 1.31 GPa into lower- and higher-wavenumber components assigned to $^{13}CO_2$ inside and outside the framework, respectively, based on comparison with pure solid $^{13}CO_2$ at 1.11 GPa. The inside-framework component shows pronounced asymmetric

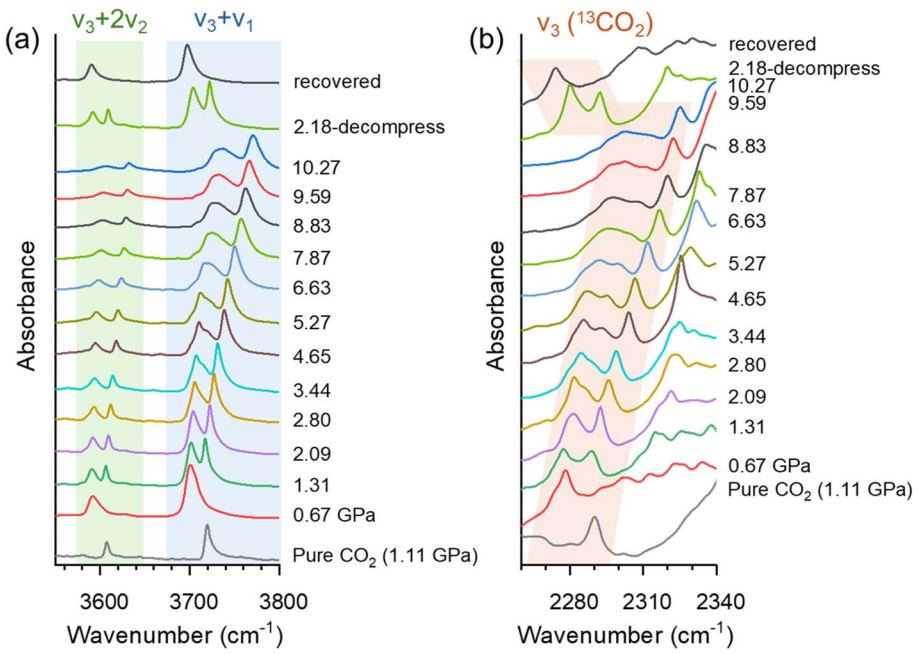

Fig. 4 Selected *in situ* FTIR spectra of CO_2-loaded ELM-11 collected on compression and decompression showing (a) the CO_2 combination-band region (3550–3800 cm^{-1}) and (b) the ν_3 region including the natural-abundance $^{13}CO_2$ band (2260–2340 cm^{-1}). Where splitting is observed, the lower- and higher-wavenumber components are assigned to CO_2 confined within the framework and excess solid CO_2 in the sample chamber, respectively.

broadening at higher pressures, supporting an increasing diversity of CO_2 binding environments, which is quantified below by deconvolution of the $^{13}CO_2$ ν_3 band.

The ν_3 band of natural-abundance $^{13}CO_2$ was deconvoluted to quantify the evolution of spectroscopically resolved adsorption environments ("sites") in CO_2-loaded ELM-11 (Fig. 5). The relative contributions of the external solid CO_2 component and the inside-framework components (Sites 1–5) obtained from the fitted areas are summarised in Table S4. The fraction assigned to solid CO_2 outside the framework decreases modestly from 31.4% (1.14 GPa) to 26.4% (3.44 GPa) and then remains approximately constant (~27–28%) at higher pressures, suggesting a small pressure-dependent redistribution of CO_2 between the pore-confined and external phases rather than a strong, monotonic uptake increase. It should be emphasised that the deconvoluted $\nu_3(^{13}CO_2)$ areas provide a semi-quantitative indicator of the relative contributions of pore-confined *versus* external CO_2 under a fixed optical geometry, but they do not constitute a direct gravimetric/volumetric adsorption isotherm (*e.g.*, band intensities can also be influenced by pressure-dependent broadening and local-field effects). Within this limitation, the modest change in the external solid-CO_2 fraction indicates that hydrostatic compression does not drive a large net transfer of additional CO_2 into the pores under the present sealed DAC conditions. Instead, the primary effect of pressure is to reorganise the binding landscape and redistribute pore-confined CO_2 among multiple environments (Sites 1–5) as new spectroscopically resolved sites emerge at elevated pressures.

Within the framework, two adsorption environments are resolved at 1.14 GPa (Sites 1 and 2), consistent with prior reports of two primary CO_2 binding regions at ambient pressure: one associated with BF_4^--proximal sites (F atoms as interaction points) and another associated with the bpy linkers.[56] A third site (Site 3) appears at 3.44 GPa, coincident with the onset of pronounced asymmetry/broadening in the confined-CO_2 bands (Fig. 4) and near the framework spectral change marked by δ(C–H) splitting at 4.65 GPa, suggesting a pressure-induced modification of the local binding landscape. At higher pressures, additional components emerge at 9.59 GPa (Site 4) and 10.27 GPa (Site 5), indicating that compression can further diversify the accessible CO_2 environments, plausibly due to increasingly compact host geometries and evolving host–guest contacts. Overall, the deconvolution demonstrates pressure-driven reorganisation of the CO_2 binding landscape in ELM-11 and motivates future modelling to map these spectroscopic sites to specific structural motifs.

Overall, the CO_2 combination-band analysis (Fig. 4) together with deconvolution of the natural-abundance $^{13}CO_2$ ν_3 band (Fig. 5) demonstrates that hydrostatic compression progressively reorganises the host–guest landscape of ELM-11. The number of spectroscopically distinguishable pore-confined CO_2 environments increases from two at 1.14–2.80 GPa to three at 3.44 GPa, with additional environments emerging above 9.59 GPa, indicating a pressure-driven diversification of accessible binding configurations within the framework. At the same time, the fraction assigned to external solid CO_2 changes only modestly with pressure (Table S4), suggesting that the

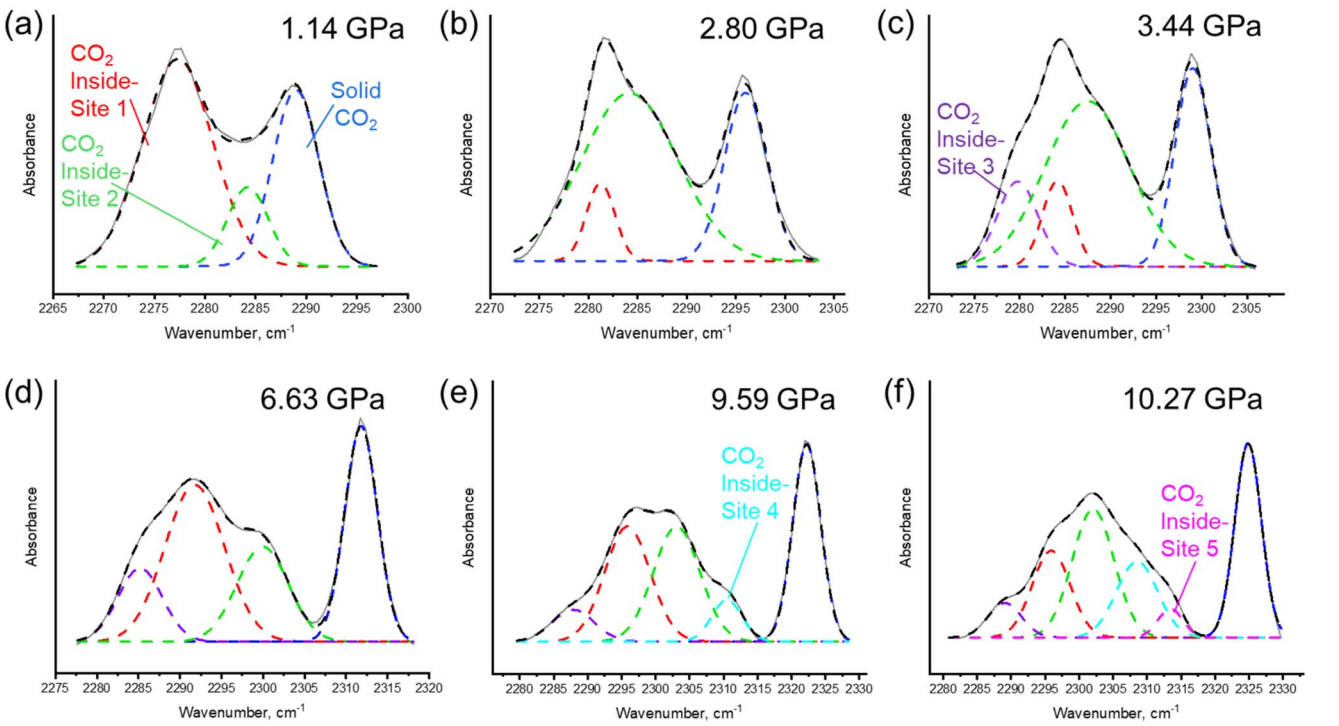

Fig. 5 Deconvolution (peak fitting) of the ν_3 band of natural-abundance $^{13}CO_2$ in the FTIR spectra of CO_2-loaded ELM-11 at (a) 1.14 GPa, (b) 2.80 GPa, (c) 3.44 GPa, (d) 6.63 GPa, (e) 9.59 GPa, and (f) 10.27 GPa. The fitted components include the contribution from external solid CO_2 in the sample chamber and multiple pore-confined $^{13}CO_2$ environments (Sites 1–5); relative areas are summarised in Table S4.

dominant effect of compression in this regime is redistribution among pore-confined environments rather than a large, monotonic net transfer from the external phase. The appearance of new sites near ~3–5 GPa coincides with observable changes in framework vibrational features (*e.g.*, δ(C–H) splitting), supporting a coupled evolution of framework configuration and CO_2 binding.

At the microscopic level, two framework degrees of freedom are likely to contribute to this binding-landscape diversification during interlayer contraction (Fig. 3c). First, the BF_4^- anions, which protrude into interlayer void regions (Fig. S1d), may reorient under compression, altering the local electrostatic environment and the geometry of F-proximal interaction regions available to CO_2. Second, the stacked-layer structure of ELM-11 contains bpy rings tilted out of the layer plane (Fig. S1d), and torsional/tilting adjustments of bpy ligands under reduced layer spacing can reshape aromatic-proximal pockets and CO_2 approach geometries. These pressure-activated conformational/orientational changes provide a plausible structural basis for the appearance of additional spectroscopically resolved pore-confined CO_2 environments. Taken together, these results establish mechanical pressure as a mechanistic probe for mapping deformation-dependent binding landscapes in flexible layered MOFs and motivate future modelling to assign Sites 1–5 to specific structural motifs (*e.g.*, BF_4^--proximal pockets *versus* bpy-adjacent regions) under compression.

A plausible reason why net pore filling does not increase strongly with pressure is that mass transport becomes diffusion-limited at high pressure: once excess CO_2 solidifies and the framework contracts, CO_2 mobility and inter-region exchange (external ↔ pore-confined) can be restricted, thereby limiting any additional uptake even if new binding pockets are generated. Consistent with this kinetic picture, our earlier high-pressure study showed that increasing temperature can promote CO_2 diffusion under high pressure,[22] supporting diffusion limitation as an important factor governing whether pressure-tuning manifests primarily as redistribution among sites rather than substantial net uptake. Therefore, systematic synergetic pressure–temperature studies represent an important future direction.

Conclusions

In this work, we establish how dehydration rewires the high-pressure mechanics of the layered ELM-11 family and how compression reshapes CO_2 binding landscapes. *In situ* synchrotron PXRD and FTIR show that hydrated pre-ELM-11 undergoes a two-stage response: interlayer-dominated compression up to 2.15 GPa, followed by a sliding-assisted deformation mode that produces a PLC → NLC crossover along *c* and a pronounced stiffening ($K_0 = 8.9 \rightarrow 49.6$ GPa). In contrast, activated ELM-11 compresses continuously from 0.12 to 4.28 GPa dominated by interlayer contraction, and principal-axis strain analysis identifies near-ZLC along X_3. These comparative findings provide a generalizable design implication for layered flexible MOFs: strong interlayer pinning interactions (*e.g.*, hydrogen-bond networks) predispose a crossover to shear/sliding once normal contraction saturates, whereas reduced interlayer pinning favors sustained contraction and near-zero-compressibility regimes. For CO_2-loaded ELM-11, *in situ* FTIR reveals a pressure-driven diversification of pore-confined CO_2 environments: two sites at 1.14–2.80 GPa, three sites at 3.44 GPa, and additional sites emerging above 9.59 GPa. The modest evolution of the external solid-CO_2 component suggests that the dominant effect of compression is redistribution among binding environments rather than a large, monotonic net uptake increase. Together, these results demonstrate that hydrostatic pressure is an effective mechanistic probe and tuning variable for linking layer mechanics (compression *vs.* sliding; near-ZLC) to host–guest binding diversity in flexible 2D MOFs. Future combined modelling and other high-pressure structural/spectroscopic studies (*e.g.*, *in situ* Raman spectroscopy and solid-state NMR) on guest-loaded states at extended *P–T* range could enable assignment of the spectroscopic sites to specific structural motifs and guide the design of layered frameworks with programmable adsorption landscapes under stress.

Author contributions

Jingyan Liu: methodology, formal analysis, investigation, writing – original draft, review & editing. Julia M. Barker: formal analysis, investigation. Jiabin Xu: formal analysis, investigation. Yining Huang: conceptualisation, supervision, funding acquisition, writing – review & editing. Yang Song: conceptualization, methodology, formal analysis, investigation, writing – review & editing, supervision, funding acquisition.

Conflicts of interest

There are no conflicts to declare.

Data availability

The data supporting this article have been included as part of the supplementary information (SI). Supplementary information: structural information, X-ray diffraction data and analysis, FTIR spectral data and analysis. See DOI: https://doi.org/10.1039/d5ta10521h.

Acknowledgements

Y. H. and Y. S. acknowledge the Natural Sciences and Engineering Research Council of Canada (NSERC) for Discovery Grants. A Leading Opportunity Fund from the Canada Foundation for Innovation (CFI) (Y. S.) is also gratefully acknowledged. This research was partially performed at the Canadian Light Source, a national research facility of the University of Saskatchewan, which is supported by the Canada Foundation for Innovation (CFI), NSERC, the Canadian Institutes of Health Research (CIHR), the Government of Saskatchewan, and the University of Saskatchewan. The authors thank Dr Graham King for technical assistance.

References

1 H. Furukawa, K. E. Cordova, M. O'Keeffe and O. M. Yaghi, *Science*, 2013, **341**, 1230444.
2 M. Ding, R. W. Flaig, H. L. Jiang and O. M. Yaghi, *Chem. Soc. Rev.*, 2019, **48**, 2783–2828.
3 I. Beurroies, M. Boulhout, P. L. Llewellyn, B. Kuchta, G. Féray, C. Serre and R. Denoyel, *Angew. Chem., Int. Ed.*, 2010, **49**, 7526–7529.
4 K. W. Chapman, G. J. Halder and P. J. Chupas, *J. Am. Chem. Soc.*, 2009, **131**, 17546–17547.
5 S. A. Moggach, T. D. Bennett and A. K. Cheetham, *Angew. Chem., Int. Ed.*, 2009, **48**, 7087–7089.
6 Y. Hu, H. Kazemian, S. Rohani, Y. Huang and Y. Song, *Chem. Commun.*, 2011, **47**, 12694–12696.
7 A. U. Ortiz, A. Boutin, K. J. Gagnon, A. Clearfield and F.-X. Coudert, *J. Am. Chem. Soc.*, 2014, **136**, 11540–11545.
8 P. Serra-Crespo, A. Dikhtiarenko, E. Stavitski, J. Juan-Alcañiz, F. Kapteijn, F.-X. Coudert and J. Gascon, *CrystEngComm*, 2015, **17**, 276–280.
9 H. Mao, J. Xu, Y. Hu, Y. Huang and Y. Song, *J. Mater. Chem. A*, 2015, **3**, 11976–11984.
10 Z. Su, Y.-R. Miao, G. Zhang, J. T. Miller and K. S. Suslick, *Chem. Sci.*, 2017, **8**, 8004–8011.
11 M. Mączka, A. Gagor, M. Ptak, W. Paraguassu, T. A. da Silva, A. Sieradzki and A. Pikul, *Chem. Mater.*, 2017, **29**, 2264–2275.
12 A. V. Chitnis, H. Bhatt, M. Mączka, M. N. Deo and N. Garg, *Dalton Trans.*, 2018, **47**, 12993–13005.
13 S. Henke, M. T. Wharmby, G. Kieslich, I. Hante, A. Schneemann, Y. Wu, D. Daisenberger and A. K. Cheetham, *Chem. Sci.*, 2018, **9**, 1654–1660.
14 S. C. McKellar, J. Sotelo, A. Greenaway, J. P. S. Mowat, O. Kvam, C. A. Morrison, P. A. Wright and S. A. Moggach, *Chem. Mater.*, 2016, **28**, 466–473.
15 L. R. Redfern, M. Ducamp, M. C. Wasson, L. Robison, F. A. Son, F.-X. Coudert and O. K. Farha, *Chem. Mater.*, 2020, **32**, 5864–5871.
16 L. Robison, R. J. Drout, L. R. Redfern, F. A. Son, M. C. Wasson, S. Goswami, Z. Chen, A. Olszewski, K. B. Idrees, T. Islamoglu and O. K. Farha, *Chem. Mater.*, 2020, **32**, 3545–3552.
17 A. Celeste, A. Paolone, J. P. Itie, F. Borondics, B. Joseph, O. Grad, G. Blanita, C. Zlotea and F. Capitani, *J. Am. Chem. Soc.*, 2020, **142**, 15012–15019.
18 S. J. Baxter, N. C. Burtch, J. D. Evans, A. D. Ready, A. P. Wilkinson and A. Schneemann, *Chem. Mater.*, 2022, **34**, 768–776.
19 Y. Hu, B. Lin, P. He, Y. Li, Y. Huang and Y. Song, *Chem. Eur. J.*, 2015, **21**, 18739–18748.
20 Y. Hu, Z. Liu, J. Xu, Y. Huang and Y. Song, *J. Am. Chem. Soc.*, 2013, **135**, 9287–9290.
21 S. Jiang, Y. Hu, S. Chen, Y. Huang and Y. Song, *Chem. Eur. J.*, 2018, **24**, 19280–19288.
22 S. Jiang, J. Liu, J. Guan, X. Du, S. Chen, Y. Song and Y. Huang, *Sci. Rep.*, 2023, **13**, 17584.
23 J. Liu, B. Li, V. Martins, Y. Huang and S. Yang, *J. Phys. Chem. C*, 2024, **128**, 8007–8015.
24 J. Liu, Z. Gao, Y. Huang and Y. Song, *Can. J. Chem.*, 2025, **103**, 566–574.
25 Y. Su, K.-i. Otake, J.-J. Zheng, P. Wang, Q. Lin, S. Kitagawa and C. Gu, *Nat. Commun.*, 2024, **15**, 2898.
26 Y. Su, K.-i. Otake, J.-J. Zheng, H. Xu, Q. Wang, H. Liu, F. Huang, P. Wang, S. Kitagawa and C. Gu, *Nat. Commun.*, 2024, **15**, 144.
27 Y. Su, K.-i. Otake, J.-J. Zheng, S. Horike, S. Kitagawa and C. Gu, *Nature*, 2022, **611**, 289–294.
28 Y. Su, J.-J. Zheng, K.-I. Otake, N. Hosono, S. Kitagawa and C. Gu, *Acc. Chem. Res.*, 2024, **57**, 3455–3464.
29 Q. Zeng, K. Wang, Y. Qiao, X. Li and B. Zou, *J. Phys. Chem. Lett.*, 2017, **8**, 1436–1441.
30 A. L. Goodwin, D. A. Keen and M. G. Tucker, *Proc. Natl. Acad. Sci. U.S.A.*, 2008, **105**, 18708–18713.
31 Y. Iwai, S. Kusumoto, R. Suzuki, M. Tachibana, K. Komatsu, T. Kikuchi, S. I. Kawaguchi, H. Kadobayashi, Y. Masubuchi, Y. Yamamoto, Y. Ozawa, M. Abe, K. Hirai, B. Le Ouay, M. Ohba and R. Ohtani, *Chem. Mater.*, 2024, **36**, 5446–5455.
32 H. Kanoh, A. Kondo, H. Noguchi, H. Kajiro, A. Tohdoh, Y. Hattori, W. C. Xu, M. Inoue, T. Sugiura, K. Morita, H. Tanaka, T. Ohba and K. Kaneko, *J. Colloid Interface Sci.*, 2009, **334**, 1–7.
33 V. Bon, I. Senkovska, D. Wallacher, A. Heerwig, N. Klein, I. Zizak, R. Feyerherm, E. Dudzik and S. Kaskel, *Microporous Mesoporous Mater.*, 2014, **188**, 190–195.
34 H. Tanaka, S. Hiraide, A. Kondo and M. T. Miyahara, *J. Phys. Chem. C*, 2015, **119**, 11533–11543.
35 A. Kondo, H. Noguchi, S. Ohnishi, H. Kajiro, A. Tohdoh, Y. Hattori, W. C. Xu, H. Tanaka, H. Kanoh and K. Kaneko, *Nano Lett.*, 2006, **6**, 2581–2584.
36 D. Li and K. Kaneko, *Chem. Phys. Lett.*, 2001, **335**, 50–56.
37 S. Onishi, T. Ohmori, T. Ohkubo, H. Noguchi, L. Di, Y. Hanzawa, H. Kanoh and K. Kaneko, *Appl. Surf. Sci.*, 2002, **196**, 81–88.
38 S. Hiraide, H. Tanaka and M. T. Miyahara, *Dalton Trans.*, 2016, **45**, 4193–4202.
39 A. J. Blake, S. J. Hill, P. Hubberstey and W.-S. Li, *J. Chem. Soc., Dalton Trans.*, 1997, **6**, 913–914.
40 A. Kondo, N. Kojima, H. Kajiro, H. Noguchi, Y. Hattori, F. Okino, K. Maeda, T. Ohba, K. Kaneko and H. Kanoh, *J. Phys. Chem. C*, 2012, **116**, 4157–4162.
41 L. Li, R. Krishna, Y. Wang, X. Wang, J. Yang and J. Li, *Eur. J. Inorg. Chem.*, 2016, **2016**, 4457–4462.
42 M. Ichikawa, A. Kondo, H. Noguchi, N. Kojima, T. Ohba, H. Kajiro, Y. Hattori and H. Kanoh, *Langmuir*, 2016, **32**, 9722–9726.
43 F. J. Sotomayor and C. M. Lastoskie, *Microporous Mesoporous Mater.*, 2020, **292**, 109371.
44 C. Prescher and V. B. Prakapenka, *High Press. Res.*, 2015, **35**, 223–230.
45 B. H. Toby and R. B. Von Dreele, *J. Appl. Crystallogr.*, 2013, **46**, 544–549.
46 R. J. Angel, M. Alvaro, J. Gonzalez-Platas and Z. Kristallogr, *Cryst. Mater.*, 2014, **229**, 405–419.

47 M. Lertkiattrakul, M. L. Evans and M. J. Cliffe, *J. Open Source Softw.*, 2023, **8**, 5556.
48 R. E. Newnham, *Properties of Materials: Anisotropy, Symmetry, Structure*, Oxford university press, 2005.
49 W. Qiu, Q. Zeng, C. Li, J. Hao and Y. Li, *J. Phys. Chem. C*, 2023, **127**, 9957–9963.
50 X. Jiang, M. S. Molokeev, L. Dong, Z. Dong, N. Wang, L. Kang, X. Li, Y. Li, C. Tian, S. Peng, W. Li and Z. Lin, *Nat. Commun.*, 2020, **11**, 5593.
51 Y. M. Xie, X. Yang, J. Shen, X. Yan, A. Ghaedizadeh, J. Rong, X. Huang and S. Zhou, *Int. J. Solids Struct.*, 2014, **51**, 4038–4051.
52 N. C. Burtch, J. Heinen, T. D. Bennett, D. Dubbeldam and M. D. Allendorf, *Adv. Mater.*, 2018, **30**, 1704124.
53 Y. Yu, Q. Zeng, Y. Chen, L. Jiang, K. Wang and B. Zou, *ACS Mater. Lett.*, 2020, **2**, 519–523.
54 S. A. Hodgson, J. Adamson, S. J. Hunt, M. J. Cliffe, A. B. Cairns, A. L. Thompson, M. G. Tucker, N. P. Funnell and A. L. Goodwin, *Chem. Commun.*, 2014, **50**, 5264–5266.
55 Q. Zeng, K. Wang and B. Zou, *Langmuir*, 2022, **38**, 9031–9036.
56 J. Xu, W. Zhang, J. Liu, J. Zhong, T. K. Sham and Y. Huang, *Chem. Eur. J.*, 2024, **30**, e202402775.